Observation of a remarkable reduction of correlation effects in $BaCr_2As_2$ by ARPES

Jayita Nayak[a], Kai Filsinger[a], Gerhard H. Fecher[a], Stanislav Chadov[a], Ján Minár[b], Emile D. L. Rienks[c,d], Bernd Büchner[c,d], Stuart P. Parkin[e,1], Jörg Fink[a,c,d,1], and Claudia Felser[a]

[a]Solid State Chemistry, Max Planck Institute for Chemical Physics of Solids, D-01187 Dresden, Germany; [b]New Technologies Research Centre, University of West Bohemia, 306 14 Pilsen, Czech Republic; [c]Institute for Solid State Physics, Leibniz Institute for Solid State and Materials Research Dresden, D-01171 Dresden, Germany; [d]Institute of Solid State Physics, Dresden University of Technology, 01062 Dresden, Germany; and [e]Nanosystems from Ions, Electrons, and Spins, Max Planck Institute for Microstructure Physics, D-01620 Halle (Saale), Germany

Contributed by Stuart P. Parkin, October 7, 2017 (sent for review February 13, 2017; reviewed by Andrea Damascelli and Charles S. Fadley)

The superconducting phase in iron-based high-T_c superconductors (FeSC), as in other unconventional superconductors such as the cuprates, neighbors a magnetically ordered one in the phase diagram. This proximity hints at the importance of electron correlation effects in these materials, and Hund's exchange interaction has been suggested to be the dominant correlation effect in FeSCs because of their multiband nature. By this reasoning, correlation should be strongest for materials closest to a half-filled 3*d* electron shell (Mn compounds, hole-doped FeSCs) and decrease for systems with both higher (electron-doped FeSCs) and lower (Cr-pnictides) 3*d* counts. Here we address the strength of correlation effects in nonsuperconducting antiferromagnetic $BaCr_2As_2$ by means of angle-resolved photoemission spectroscopy (ARPES) and first-principles calculations. This combination provides us with two handles on the strength of correlation: First, a comparison of the experimental and calculated effective masses yields the correlation-induced mass renormalization. In addition, the lifetime broadening of the experimentally observed dispersions provides another measure of the correlation strength. Both approaches reveal a reduction of electron correlation in $BaCr_2As_2$ with respect to systems with a 3*d* count closer to five. Our results thereby support the theoretical predictions that Hund's exchange interaction is important in these materials.

correlated systems | transition metal pnictides | superconductivity | ARPES

The discovery of the high-T_c iron-based superconductors (FeSC) (1) has stimulated strong research activities in this field (2). Similar to the cuprates and other unconventional superconductors, in the phase diagram of the temperature vs. control parameter, the superconducting dome appears at the end of an antiferromagnetic region. Therefore, it seems likely that correlation effects may be important for the FeSCs. On the other hand, different from the cuprates, the parent compounds of the FeSCs are not Mott–Hubbard insulators but metallic. Furthermore, a multiplet analysis of X-ray absorption edges at the Fe $2p$ level yielded values for the on-site Coulomb interaction U at the iron sites smaller than 2 eV, which is less than the bandwidth of the iron bands $W = 5$ eV (3, 4). This led to the conclusion that FeSCs are only moderately correlated systems.

Theoretical studies (5–10), however, pointed out that, due to the multiorbital electronic structure together with Hund's exchange interaction J_H, correlation effects are important. According to these studies, correlation effects should be strongest for compounds with a nearly half-filled $3d$ electron shell (e.g., Mn compounds and hole-doped ferropnictides), and these effects should be smaller for compounds having a $3d$ count closer to 6 (electron-doped ferropnictides) or compounds having a $3d$ count closer to 4 (e.g., Cr–pnictides).

There are several experimental studies of the mass enhancement as a function of the $3d$ count in the ferropnictides which confirm these predictions (11, 12). These studies, however, suffer from a large variance of the experimental results and in the case of transport and thermal property data they cannot be assigned to particular bands. Additional angle-resolved photoemission spectroscopy (ARPES) data on the scattering rate of inner hole pockets as a function of $3d$ count (13) show a strong incoherence of the charge carriers in the hole-doped ferropnictides and more coherence for the electron-doped compounds. Incoherence of the charge carriers is caused by strong correlation effects while coherence is related to weaker correlation effects.

The theoretical results predicting a symmetry relative to the $3d$ count of five for a half-filled $3d$ shell led to the speculation that high-T_c superconductivity may also appear in Cr–pnictide compounds (14, 15). However, to our knowledge no superconductivity has been observed in $BaCr_2As_2$. Mn and Cr doping of $BaFe_2As_2$ furthermore turned out to be detrimental to superconductivity (16). Singh et al. (17) predicted that $BaCr_2As_2$ exhibits an enhanced mass renormalization and stronger Cr–As covalency compared with the Fe-based superconductors. Very recently, the discovery of superconductivity in $K_2Cr_2As_3$ (18) and high-pressure superconductivity in CrAs (19) sparked renewed interest in exploring the effect of Cr doping in iron-based superconductors.

In this contribution we study the question of whether for pnictide compounds with a $3d$ count smaller than five, correlation effects increase or decrease. This is a fundamental question in correlated condensed-matter physics. The answer could confirm the importance of Hund's exchange interaction J_H for the coherence of the charge carriers in these compounds and it could confirm or deny the existence of a "Hund's metal" (5).

Significance

By varying the 3*d* transition metal element in the family of the high-temperature superconducting pnictide family, the role of electron–electron correlations can be probed. Here we report the growth of single crystals of the antiferromagnetic compound $BaCr_2As_2$ that permit angle-resolved photoemission studies to determine its electronic structure. We show, from measurements of the electron's effective mass and the lifetime broadening of the electron energy bands, that the electron–electron correlation strength is determined in large part by a Hund's exchange interaction. Our results help us understand the subtle competition between the antiferromagnetic ground state of the Cr, Mn, and Fe pnictides and the superconducting ground state that has been found only in the iron pnictides to date.

Author contributions: B.B. and C.F. designed research; J.N., K.F., G.H.F., S.C., J.M., E.D.L.R., and J.F. performed research; J.N., K.F., G.H.F., S.C., J.M., and E.D.L.R. analyzed data; and J.N., J.F., and S.P.P. wrote the paper.

Reviewers: A.D., British Columbia University; and C.S.F., University of California, Davis and Lawrence Berkeley National Laboratory.

The authors declare no conflict of interest.

[1]To whom correspondence may be addressed. Email: stuart.parkin@mpi-halle.mpg.de or J.Fink@ifw-dresden.de.

We use ARPES (20) to yield information on the mass renormalization, related to the real part of the self-energy $\Re\Sigma$, and on the scattering rate or the lifetime broadening Γ, which is related to the imaginary part of the self-energy $\Im\Sigma$. We point out that $\Re\Sigma$ and $\Im\Sigma = \Gamma/2$ are related via the Kramers–Kronig relation. Since we obtain not only energy-dependent, but also momentum-dependent information, ARPES provides information on the orbital and band dependence of the strength of the correlation effects. The experimental results are compared with band structure calculations in the local density approximation (LDA). The results on the mass renormalization as well as the scattering rate indicate a decrease of the correlation effects for compounds with a $3d$ count smaller than five, which confirms the theoretical predictions for the importance of Hund's exchange interaction for compounds with an electron configuration which is close to a half-filled $3d$ shell.

Results

In Fig. 1 *A* and *B* we present the structure and the Brillouin zone (BZ) of $BaCr_2As_2$, respectively. In Fig. 1*C* we show the experimental geometry of the present ARPES experiment (*Methods*). In addition, we present in Fig. 1 *D* and *E* ARPES data of $BaCr_2As_2$ near the $k_z = 0$ plane, using s polarized (vertically polarized) photons with the energy $h\nu = 70$ eV. For the calculation of the k_z values we use an inner potential of $V = 15$ eV (21). Fig. 1*D* shows the experimental Fermi surface map. In Fig. 1*E* we present an energy-momentum distribution map measured along the $S' - \Gamma - S'$ direction (parallel to k_y), where $S' = \frac{\pi}{a}(0, \pm 1, 0)$. Three hole pockets at the center of the BZ are visible in Fig. 1 *D* and *E*. The derived Fermi wave vectors along the $S' - \Gamma - S'$ direction are presented in Table 1 and compared with values obtained from an LDA band structure calculation which is depicted in Fig. 1*G*. The three hole pockets near Γ are marked by I, II, and III. In Fig. 1*F* we present a calculation of the Fermi surface in the $k_z = 0$ plane. In Fig. 1*H* we show a calculation of the corresponding photoemission intensity, using the LDA together with matrix elements and final state effects (*Methods*). The calculated Fermi surface (Fig. 1*F*) as well as the intensity distribution agrees reasonably with the experimental ARPES Fermi surface and intensities. Small differences may be explained by the different surface termination in the experiment, which is usually assumed to be at low temperatures a half-occupied disordered Ba layer (22, 23), and that used in the calculations, which was chosen to be As terminated. Additional differences between the experiment and the calculations may be caused by a misaligned crystal (*Methods*). According to the calculations, the inner hole pocket at Γ (Fig. 1*G*) has predominantly Cr $3d_{xy}$ and As $4p_z$ orbital character. The middle and the outer hole pockets near Γ are dominated by Cr $3d_{xz/yz}$ and $3d_{z^2}$ states and have fewer contributions from As $4p_x$ and $4p_y$ states.

The orbital character of the inner hole pocket, predicted from the LDA calculations, is in line with the experimentally observed strong intensity along the [010] direction (Fig. 1 *D* and *E*) which is expected for s polarized photons and an odd wave function (here with $3d_{xy}$ orbital character) relative to the horizontal scattering plane, but not for p polarized photons (24).

From the ARPES data along the $S' - \Gamma - S'$ direction (Fig. 1*B*) we derive the "renormalized" Fermi velocities v_F^* for the three hole pockets which are listed in Table 1. These values are compared with the Fermi velocities v_F^0 derived from LDA band structure calculations. The calculated mass renormalizations $m^*/m^0 = v_F^0/v_F^*$ (25) for the three hole pockets are presented in Table 1 as well.

Analogous results to those in Fig. 1, but for $h\nu = 88$ eV, are shown in Fig. 2. This photon energy corresponds to the Z point in the BZ where $Z = (0, 0, \frac{\pi}{c})$ and c is the lattice constant

Table 1. Fermi wave vectors k_F [Å^{-1}], Fermi velocities v_F [eVÅ], mass renormalizations m^*/m^0, and slopes β of the imaginary part of the self-energy for the hole pockets in $BaCr_2As_2$

Hole pocket	Inner	Middle	Outer
k_F from ARPES $S' - \Gamma - S'$	0.23 ± 0.05	0.48 ± 0.05	0.61 ± 0.05
k_F from LDA $S' - \Gamma - S'$	0.25	0.55	0.62
k_F from ARPES $S - Z - S$	—	0.48 ± 0.05	0.62 ± 0.05
k_F from LDA $S - Z - S$	—	0.53	0.68
v_F from ARPES $S' - \Gamma - S'$	1.65 ± 0.10	1.47 ± 0.10	0.84 ± 0.10
v_F from LDA $S' - \Gamma - S'$	1.33	1.03	1.01
v_F from ARPES $S - Z - S$	—	1.03 ± 0.10	1.00 ± 0.10
v_F from LDA $S - Z - S$	—	1.06	1.08
m^*/m^0 $S' - \Gamma - S'$	0.81 ± 0.05	0.70 ± 0.05	1.20 ± 0.14
m^*/m^0 $S - Z - S$	—	1.03 ± 0.10	1.08 ± 0.10
β $S' - \Gamma - S'$	0.35 ± 0.10	0.39 ± 0.10	0.63 ± 0.10
β $S - Z - S$	—	0.14 ± 0.10	0.54 ± 0.10

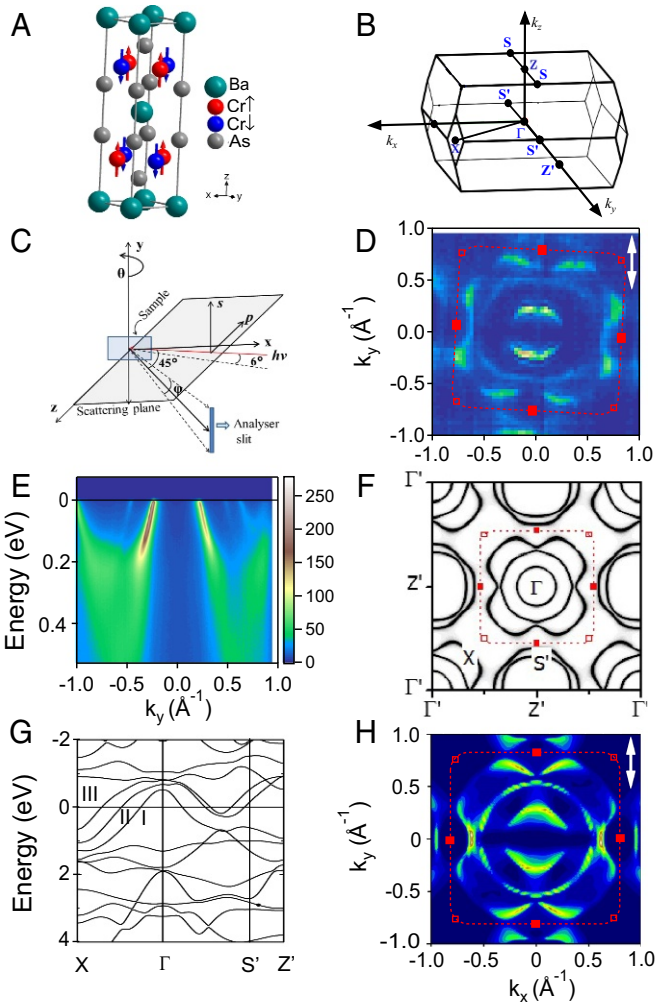

Fig. 1. (*A*) Structure of $BaCr_2As_2$. (*B*) The corresponding Brillouin zone. (*C*) Experimental geometry of the ARPES experiment. (*D* and *E*) ARPES intensity and energy-momentum distribution map along $S' - \Gamma - S'$ parallel to k_y, using s polarized photons with the energy of 70 eV. (*F*) Calculated Fermi surface map in the $k_z = 0$ plane. (*G*) LDA band structure calculation along $X - \Gamma - S' - Z'$. (*H*) Calculated photoemission intensity for experimental conditions as described for *D*. The photon polarization is indicated by a white double arrow and the Brillouin zone is marked by a red dashed line.

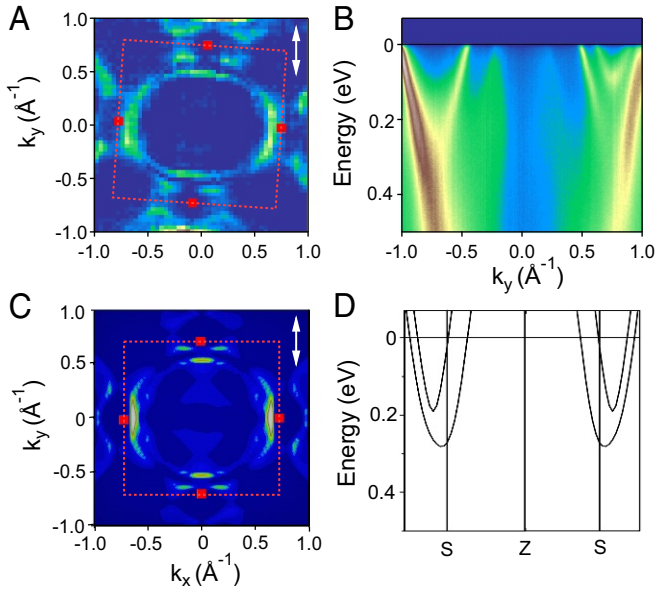

Fig. 2. Analogous data to those in Fig. 1 but for a photon energy of 88 eV photons yielding data in the $k_z = \frac{\pi}{c}$ plane. (*A*) ARPES intensity distribution. (*B*) ARPES energy-momentum distribution data along $S' - Z - S'$ parallel to k_y. (*C*) Calculated photoemission intensity for experimental conditions as described for *A*. (*D*) LDA band structure calculation of $BaCr_2As_2$ along $S - Z - S$.

perpendicular to the CrAs layers. The energy-momentum distribution map, presented in Fig. 2*B*, is now measured along the $S - Z - S$ line (Fig. 1*B*). The inner hole pocket, now near the Z point, is not observed (Fig. 2 *A* and *B*). This is in line with the calculated band structure (Fig. 1*G*), which indicates that near the corresponding Z' point, band I has moved to energies 1 eV below the Fermi level. Moreover, the calculated band structure depicted in Fig. 2*D* shows no inner hole pocket near Z. The apparent elongation of the middle hole pocket (Fig. 2*A*) results from a superposition of the middle and the outer hole pocket, where the middle hole pocket has a large intensity along k_x while the outer hole pocket has a larger intensity along k_y. This is clearly observed in the corresponding photoemission intensity calculation shown in Fig. 2*C*. The experimental k_F values along the $S - Z - S$ line are listed in Table 1. They are close to values derived from the density functional theory (DFT) calculations also shown in Table 1. In Table 1 we also present the corresponding Fermi velocities and the mass renormalizations.

Fig. 3 shows ARPES data taken with horizontally p polarized light. The Fermi surface map for $k_z = 0$ (Fig. 3*A*) obtained using 70-eV photons also exhibits three hole pockets. The corresponding k_F values are quite similar to those obtained with s polarization. The corresponding calculated Fermi surface map, shown in Fig. 3*C*, is in reasonable agreement with the experiment. The energy-momentum distribution map depicted in Fig. 3*B*, measured along $S' - \Gamma - S'$, exhibits all three hole pockets. In the energy-momentum distribution map (Fig. 3*D*), measured along the $S - Z - S$ line, the inner hole pocket is also absent as expected from the band structure calculation. The spectra acquired with p polarized light (Fig. 3 *B* and *D*) exhibit the presence of additional bands below 0.15 eV that are absent when using s polarization. These bands are possibly related to Cr $3d_{z^2}$ bands. In the spectra measured along the $S' - \Gamma - S'$ line using s (Fig. 1 *D* and *E*) and p polarized photons (Fig. 3 *A* and *B*), all three hole pockets are clearly visible. This is different from the hole- and electron-doped iron–pnictide compounds, where the intensity of the inner and the middle hole pocket changed upon changing the photon polarization (13, 21, 26). This means that in $BaCr_2As_2$ both even and odd parity orbitals contribute to each band, indicating a stronger hybridization between the orbitals which was already predicted in ref. 17.

The measured photoelectron spectra were further analyzed to extract the electron scattering rates. We performed a fitting of the momentum distribution curves by Lorentzians. The maxima of the Lorentzians, derived from constant energy cuts, result in the dispersions to which parabolic bands were fitted shown in Fig. 4 *A* and *C* by the white dashed lines where we present ARPES data measured with p polarized photons parallel to k_y along $S' - \Gamma - S'$ and $S - \Gamma - S$, respectively. In Fig. 4 *A* and *C* we also added the dispersions derived from the band structure calculation (shown by red dashed lines) to demonstrate the small mass renormalization in these compounds. The differences between experiment and calculations, which occur in particular for the outer hole pockets, may be explained by misaligned samples and by the differences between the real surface termination and that assumed in the calculations (*Methods*). The width of the Lorentzians represents the lifetime broadening. The half width at half maximum of the momentum distribution curves multiplied by the renormalized velocities provides the imaginary part of the self-energy $\Im\Sigma(E)$ (Fig. 4 *B* and *D*). In the accessible energy range, which is limited at low energy by the finite energy and momentum resolution and by a finite elastic scattering rate and at high energies by the presence of other bands, we observe a linear increase of $\Im\Sigma(E)$. This is a hallmark of a non–Fermi-liquid regime, similar to what has been observed in the ferropnictides. In the evaluated region the imaginary part of the self-energy can be approximated by $\Im\Sigma(E) = \alpha + \beta E$. α is determined by elastic scattering from impurities at the surface and in the bulk. Also a finite energy and momentum resolution contributes to the experimental α values, which are on the order of 10–20 meV. β is determined by inelastic scattering processes

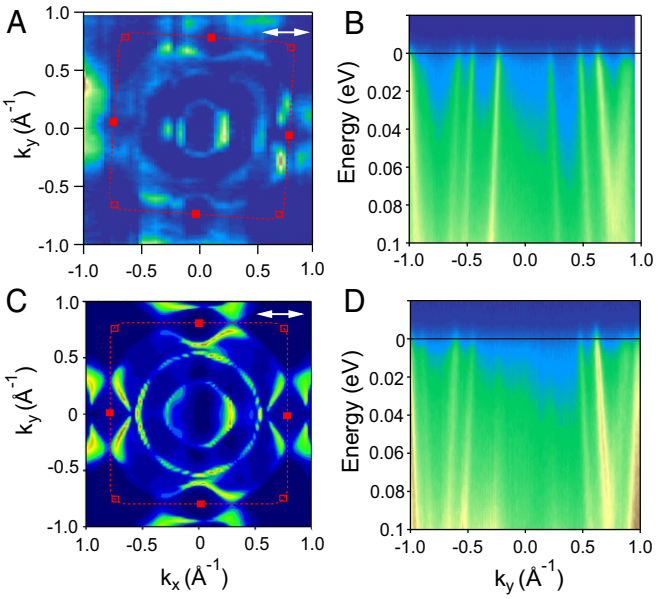

Fig. 3. Similar data to those in Figs. 1 and 2 but measured with *p* polarized photons. (*A* and *C*) ARPES intensity and calculated photoemission intensity in the $k_z = 0$ plane, using *p* polarized 70-eV photons, respectively. The polarization of the photons is indicated by a double arrow. (*B* and *D*) Energy-momentum distribution maps along $S' - \Gamma - S'$ and $S - Z - S$ parallel to the k_y axis, recorded with photon energies of 70 eV ($k_z = 0$) and 88 eV ($k_z = \pi$), respectively.

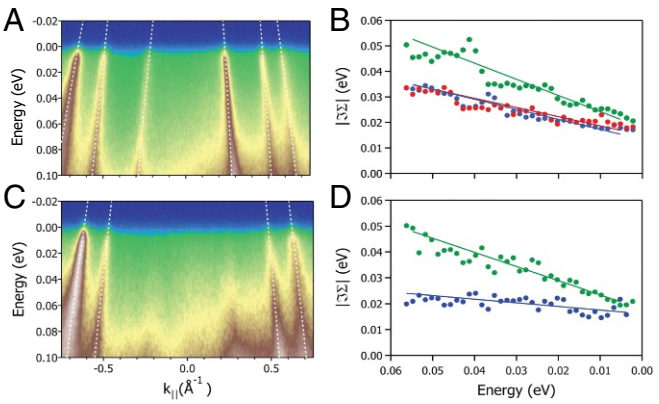

Fig. 4. Energy-momentum distribution map and imaginary part of the self-energy $\Im\Sigma(E)$ from ARPES experiments. (*A*) Map along the $S' - \Gamma - S'$ direction, measured using *p* polarized photons. White dashed curves show dispersions derived from ARPES data and red dashed curves show dispersions from band structure calculation. (*B*) $\Im\Sigma$ as a function of energy for the three hole pockets together with a linear fit; red, blue, and green data correspond to the inner, middle, and outer hole pockets, respectively. (*C* and *D*) Similar to *A* and *B* but acquired along the $S - Z - S$ direction.

due to electron–electron interaction (26). The β values derived from the ARPES data shown in Fig. 4 *B* and *D* are presented in Table 1.

Discussion

In the electron- and hole-doped ferropnictides and in ferrochalcogenides, not only a mass renormalization has been derived from ARPES spectra, but also a band shift has been observed, which leads to a correlation-induced complex change of the Fermi wave vectors relative to Fermi wave vectors derived from LDA band structure calculations (27). Theoretical work on this phenomenon has been published in refs. 5, 28, and 29. The proximity of the ARPES Fermi wave vectors in $BaCr_2As_2$ to the calculated ones is a first indication that correlation effects in $BaCr_2As_2$ are smaller than in the iron-based superconductors. This is supported also by the observation that different from the more correlated ferropnictides, where due to correlation effects the $3d_{xy}$ pocket is shifted above the Fe $3d_{xz/yz}$ hole pockets (29), in $BaCr_2As_2$, due to reduced correlation effects, the $3d_{xy}$ pocket remains below the $3d_{xz/yz}$ pockets.

Next we compare the mass renormalization observed in the present study on $BaCr_2As_2$ with those derived from ARPES, quantum oscillations, and thermal properties on the Fe-based compounds (11). In the latter compounds mass renormalization values between 2 and 4 have been presented for most of the ferropnictides but in some studies values up to 18 have been published (11). The values derived in the present study for $BaCr_2As_2$ are close to 1, indicating a rather small mass renormalization due to correlation effects mediated by electron–electron interaction. In this context we mention a recent study of the band renormalization in $BaMn_2As_2$ and $BaMn_2Sb_2$ in which also a negligible band structure renormalization has been observed (30).

Next we discuss the derived scattering rates for the charge carriers in $BaCr_2As_2$. The highest β values in electron-doped and P-substituted ferropnictides are about 0.9 (26) while in the hole-doped compounds β has a value of about 1.7 (13). In $BaCr_2As_2$ the highest value, $\beta = 0.63$ is considerably reduced compared with the Fe compounds. Since the scattering rate in a local approximation is related to the effective on-site Coulomb interaction U_{eff}, comprising also the Hund's exchange interaction J_H (13, 26), the reduced scattering rates could signal a reduced U_{eff} and thus weaker correlation effects in the Cr-based compound.

On the other hand, the reduced scattering rates may be also influenced by the band structure which is different from that of the ferropnictides. There the largest scattering rates are caused by the nesting between sections on the hole pockets and on the electron pockets having the same orbital character (13, 26, 31). In $BaCr_2As_2$, however, the corresponding electron pocket is not available for scattering processes, since due to the reduced total number of $3d$ electrons, it has moved far above the Fermi level. Nevertheless the β values derived for the individual hole pockets in $BaCr_2As_2$ have some similarities to those in ferropnictides. The β value for the inner hole pocket at Γ, having predominantly Cr $3d_{xy}$ orbital character, is smaller than those derived from the other pockets which have predominantly $3d_{xz/yz}$ orbital character. This is similar to the ferropnictides where the β value for sections of the Fermi surface having predominantly $3d_{yz}$ character is larger than those having predominantly $3d_{xy}$ orbital character. Furthermore, similar to the ferropnictide, there is some difference in the scattering rates between the non-$3d_{xy}$ pockets. It would be certainly interesting to understand these differences on the basis of theoretical calculations.

One may think that the reduced correlation effects in $BaCr_2As_2$ may be related to the antiferromagnetic order of this compound. However, in a recent study of Mn compounds (30) it was pointed out that in $BaFe_2As_2$ the strength of the correlation effects does not change when moving from the paramagnetic to the antiferromagnetic phase (32). This statement is in line with DFT+density mean-field theory (DMFT) calculations for the mass renormalization in $BaFe_2As_2$ which predicted only a minor reduction when going from the paramagnetic to the antiferromagnetic state (33).

The reduction of the correlation effects in $BaCr_2As_2$ relative to the hole-doped ferropnictides, derived from the real (related to the mass enhancement) and the imaginary part (related to the scattering rate) of the self-energy, perfectly agrees with the predictions derived from DFT+DMFT calculations and the conception of a Hund's metal, which leads to strong scattering rates connected with incoherence for the half-filled $3d$ shell. There U_{eff} is enhanced due to the additional effects of Hund's exchange interaction J_H. On the other hand when moving away from half filling to lower or higher $3d$ counts, according to these calculations, U_{eff} is reduced by the Hund's exchange interaction. This would lead to reduced correlation effects and more coherent quasi-particles for smaller or larger filling of the $3d$ shell. The present study on the Cr compound showing a reduced scattering rate and a negligible band renormalization, compared with hole-doped ferropnictides, confirms the proposed theoretical concept of Hund's metals. Similar work coming to comparable conclusions was published after the submission of our work (34).

Methods

ARPES has been performed on $BaCr_2As_2$ single crystals. The details of the single-crystal synthesis and characterization are described elsewhere (35). The ARPES experiments were carried out at the UE 112–PGM2b beamline of the synchrotron radiation facility BESSYII at Helmholtz-Zentrum Berlin, using the 1^3 ARPES end station that is equipped with a Scienta R4000 energy analyzer. All measurements were performed at a temperature of 1 K. The photon energies were varied from 50 eV to 110 eV, using both *s* and *p* polarization as defined in Fig. 1C. The mirror plane $(0; 0; \pi) - \Gamma - (\pi; 0; 0) = (x; 0; z)$ was turned into the scattering plane. Using this geometry, cuts along the k_y direction for various k_x values could be recorded by changing the polar angle Θ from nearly normal incidence to more grazing incidence. A correct alignment of the crystal is difficult since in the 1^3 ARPES 1-K manipulator the crystal cannot be tilted. Furthermore, the azimuthal rotation is manual and causes an error of $\approx 4^\circ$. The total energy resolution was $\sim$4 meV and the angular resolution was 0.2°. The measurements were performed on crystals which were cleaved in situ at low temperatures. From ARPES experiments (22) and from band structure

calculations (23) it was concluded that at low temperatures the surface of a cleaved $BaFe_2As_2$ crystal is terminated by a half-occupied disordered Ba layer. This disordered surface termination is difficult to treat in the band structure calculations and therefore we used in the present calculations a surface which is terminated by an As layer. This resulted in enhanced surface states which were finally removed from the presented theoretical data. In this way we achieve results which should be close to results expected for the surface used in the experiment.

The ab initio calculations are based on the multiple-scattering approach [Korringa–Kohn–Rostoker (KKR) method] and density functional theory as implemented in the Munich SPR-KKR program package (36, 37). As a first step of our investigations we performed self-consistent calculations for a 3D bulk as well as a 2D semiinfinite surface of antiferromagnetic $BaCr_2As_2$ within the screened KKR formalism. The first-principles analysis of the photoelectron spectroscopy is based on the fully relativistic one-step model of photoemission in its spin-density matrix formulation (38, 39), which includes all matrix–element effects, multiple scattering in the initial and final states, and all surface-related effects in the excitation process. All photoemission calculations were performed using the geometry and parameters of the experiment, including photon energy and polarization.

ACKNOWLEDGMENTS. We acknowledge BESSY for providing experimental time with Proposal No. 16103260. J.F., B.B., and C.F. acknowledge support by the German Research Foundation through the priority program 1458. J.M. acknowledges support by the European Regional Development Fund (ERDF) and Ministry of Education, Youth, and Sports of Czech Republic, through the project Computational and Experimental Design of Advanced Materials with New Functionalities (CZ.02.1.01/0.0/0.0/15 003/0000358).

1. Kamihara Y, Watanabe T, Hirano M, Hosono H (2008) Iron-based layered superconductor $LaO_{1-x}F_xFeAs(x = 0.05 - 0.12)$ with $T_c = 26K$. *J Am Chem Soc* 130:3296–3297.
2. Johnston DC (2010) The puzzle of high temperature superconductivity in layered iron pnictides and chalcogenides. *Adv Phys* 59:803–1061.
3. Kroll T, et al. (2008) Electronic structure of $LaFeAsO_{1-x}F_x$ from x-ray absorption spectroscopy. *Phys Rev B* 78:220502.
4. Yang WL, et al. (2009) Evidence for weak electronic correlations in iron pnictides. *Phys Rev B* 80:014508.
5. Haule K, Shim JH, Kotliar G (2008) Correlated electronic structure of $LaO_{1-x}F_xFeAs$. *Phys Rev Lett* 100:226402.
6. Aichhorn M, et al. (2009) Dynamical mean-field theory within an augmented plane-wave framework: Assessing electronic correlations in the iron pnictide LaFeAsO. *Phys Rev B* 80:085101.
7. Aichhorn M, Biermann S, Miyake T, Georges A, Imada M (2010) Theoretical evidence for strong correlations and incoherent metallic state in FeSe. *Phys Rev B* 82:064504.
8. de'Medici L, Mravlje J, Georges A (2011) Janus-faced influence of Hund's Rule coupling in strongly correlated materials. *Phys Rev Lett* 107:256401.
9. Werner P, et al. (2012) Satellites and large doping and temperature dependence of electronic properties in hole-doped $BaFe_2As_2$. *Nat Phys* 8:331–337.
10. de Medici L (2015) *Weak and Strong Correlations in Fe Superconductors in Iron-Based Superconductivity*, eds Johnson PD, Xu G, Yin WG (Springer, Cham, Switzerland), pp 409–441.
11. van Roekeghem A, Richard P, Ding H, Biermann S (2016) Spectral properties of transition metal pnictides and chalcogenides: Angle-resolved photoemission spectroscopy and dynamical mean-field theory. *C R Phys* 17:140–163.
12. Hardy F, et al. (2016) Strong correlations, strong coupling, and s -wave superconductivity in hole-doped $BaFe_2As_2$ single crystals. *Phys Rev B* 94:205113.
13. Fink J, et al. (2017) Experimental evidence for importance of Hund's exchange interaction for incoherence of charge carriers in iron-based superconductors. *Phys Rev B* 95:144513.
14. Pizarro JM, Calderón MJ, Liu J, Muñoz MC, Bascones E (2017) Strong correlations and the search for high-T_c superconductivity in chromium pnictides and chalcogenides. *Phys Rev B* 95:075115.
15. Edelmann M, Sangiovanni G, Capone M, de'Medici L (2017) Chromium analogs of iron-based superconductors. *Phys Rev B* 95:205118.
16. Sefat AS, et al. (2009) Absence of superconductivity in hole-doped $BaFe_{2-x}Cr_xAs_2$ single crystals. *Phys Rev B* 79:224524.
17. Singh DJ, et al. (2009) Itinerant antiferromagnetism in $BaCr_2As_2$: Experimental characterization and electronic structure calculations. *Phys Rev B* 79:094429.
18. Bao JK, et al. (2015) Superconductivity in quasi-one-dimensional $K_2Cr_3As_3$ with significant electron correlations. *Phys Rev X* 5:011013.
19. Wu W, et al. (2014) Superconductivity in the vicinity of antiferromagnetic order in CrAs. *Nat Commun* 5:5508.
20. Damascelli A, Hussain Z, Shen ZX (2003) Angle-resolved photoemission studies of the cuprate superconductors. *Rev Mod Phys* 75:473–541.
21. Thirupathaiah S, et al. (2010) Orbital character variation of the Fermi surface and doping dependent changes of the dimensionality in $BaFe_{2-x}Co_xAs_2$ from angle-resolved photoemission spectroscopy. *Phys Rev B* 81:104512.
22. van Heumen E, et al. (2011) Existence, character, and origin of surface-related bands in the high temperature iron pnictide superconductor $BaFe_{2-x}Co_xAs_2$. *Phys Rev Lett* 106:027002.
23. Lankau A, et al. (2010) Absence of surface states for LiFeAs investigated using density functional calculations. *Phys Rev B* 82:184518.
24. Fink J, et al. (2009) Electronic structure studies of $BaFe_2As_2$ by angle-resolved photoemission spectroscopy. *Phys Rev B* 79:155118.
25. Mahan G (2000) *Many-Particle Physics* (Springer, Boston).
26. Fink J, et al. (2015) Non-fermi-liquid scattering rates and anomalous band dispersion in ferropnictides. *Phys Rev B* 92:201106.
27. Maletz J, et al. (2014) Unusual band renormalization in the simplest iron-based superconductor $FeSe_{1-x}$. *Phys Rev B* 89:220506.
28. Ortenzi L, Cappelluti E, Benfatto L, Pietronero L (2009) Fermi-surface shrinking and interband coupling in iron-based pnictides. *Phys Rev Lett* 103:046404.
29. Lee G, et al. (2012) Orbital selective fermi surface shifts and mechanism of high T_c superconductivity in correlated AFeAs(A = Li, Na). *Phys Rev Lett* 109: 177001.
30. Zhang WL, et al. (2016) Angle-resolved photoemission observation of Mn-pnictide hybridization and negligible band structure renormalization in $BaMn_2As_2$ and $BaMn_2Sb_2$. *Phys Rev B* 94:155155.
31. Avigo I, et al. (2017) Electronic structure and ultrafast dynamics of FeAs-based superconductors by angle- and time-resolved photoemission spectroscopy. *Phys Status Solidi B* 254:1600382.
32. Richard P, et al. (2010) Observation of Dirac cone electronic dispersion in $BaFe_2As_2$. *Phys Rev Lett* 104:137001.
33. Yin ZP, Haule K, Kotliar G (2011) Kinetic frustration and the nature of the magnetic and paramagnetic states in iron pnictides and iron chalcogenides. *Nat Mater* 10: 932–935.
34. Richard P, et al. (2017) Is $BaCr_2As_2$ symmetrical to $BaFe_2As_2$ with respect to half 3*d* shell filling? *Phys Rev B* 95:184516.
35. Filsinger KA, et al. (2017) Antiferromagnetic structure and electronic properties of $BaCr_2As_2$ and $BaCrFeAs_2$. *Phys Rev B* 95:184414.
36. Ebert H, Ködderitzsch D, Minár J (2011) Calculating condensed matter properties using the KKR-Green's function method—recent developments and applications. *Rep Prog Phys* 74:096501.
37. Ebert H, et al. (2016) *The Munich SPR-KKR Package*, version 6.3. Available at olymp.cup.uni-muenchen.de/ak/ebert/SPRKKR. Accessed October 26, 2017.
38. Braun J, et al. (2014) Exceptional behavior of d-like surface resonances on W(110): The one-step model in its density matrix formulation. *New J Phys* 16:015005.
39. Minár J, Braun J, Mankovsky S, Ebert H (2011) Calculation of angle-resolved photo emission spectra within the one-step model of photo emission—Recent developments. *J Electron Spectros Relat Phenom* 184:91–99.